Downloaded from orbit.dtu.dk on: Apr 21, 2025

DTU Library

Improving the accuracy of temperature measurement on TEM samples using plasmon energy expansion thermometry (PEET)

Addressing sample thickness effects

Yang, Yi Chieh; Serafini, Luca; Gauquelin, Nicolas; Verbeeck, Johan; Jinschek, Joerg R.

Published in:
Ultramicroscopy

Link to article, DOI:
10.1016/j.ultramic.2025.114102

Publication date:
2025

Document Version
Publisher's PDF, also known as Version of record

Link back to DTU Orbit

Citation (APA):
Yang, Y. C., Serafini, L., Gauquelin, N., Verbeeck, J., & Jinschek, J. R. (2025). Improving the accuracy of temperature measurement on TEM samples using plasmon energy expansion thermometry (PEET): Addressing sample thickness effects. *Ultramicroscopy*, *270*, Article 114102. https://doi.org/10.1016/j.ultramic.2025.114102

General rights
Copyright and moral rights for the publications made accessible in the public portal are retained by the authors and/or other copyright owners and it is a condition of accessing publications that users recognise and abide by the legal requirements associated with these rights.

- Users may download and print one copy of any publication from the public portal for the purpose of private study or research.
- You may not further distribute the material or use it for any profit-making activity or commercial gain
- You may freely distribute the URL identifying the publication in the public portal

If you believe that this document breaches copyright please contact us providing details, and we will remove access to the work immediately and investigate your claim.

Ultramicroscopy 270 (2025) 114102

Contents lists available at ScienceDirect

Ultramicroscopy

journal homepage: www.elsevier.com/locate/ultramic

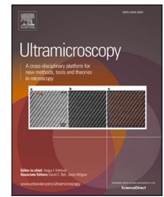

Improving the accuracy of temperature measurement on TEM samples using plasmon energy expansion thermometry (PEET): Addressing sample thickness effects

Yi-Chieh Yang [a,1], Luca Serafini [b,c,1], Nicolas Gauquelin [b,c], Johan Verbeeck [b,c], Joerg R. Jinschek [a,*]

[a] National Centre for Nano Fabrication and Characterization (DTU Nanolab), Technical University of Denmark (DTU), Kgs. Lyngby, Denmark
[b] Electron Microscopy for Materials Science (EMAT), University of Antwerp, Antwerp, Belgium
[c] NANOlab Center of Excellence, University of Antwerp, Antwerp, Belgium

A R T I C L E I N F O

Keywords:
Thermometry
Bulk plasmon energy
In-situ heating
Tungsten
STEM-EELS
FIB

A B S T R A C T

Advances in analytical scanning transmission electron microscopy (STEM) and in microelectronic mechanical systems (MEMS) based microheaters have enabled *in-situ* materials' characterization at the nanometer scale at elevated temperature. In addition to resolving the structural information at elevated temperatures, detailed knowledge of the local temperature distribution inside the sample is essential to reveal thermally induced phenomena and processes. Here, we investigate the accuracy of plasmon energy expansion thermometry (PEET) as a method to map the local temperature in a tungsten (W) lamella in a range between room temperature and 700 °C. In particular, we address the influence of sample thickness in the range of a typical electron-transparent TEM sample (from 30 nm to 70 nm) on the temperature-dependent plasmon energy. The shift in plasmon energy, used to determine the local sample temperature, is not only temperature-dependent, but in case of W also seems thickness-dependent in sample thicknesses below approximately 60 nm. It is believed that the underlying reason is the high susceptibility of the regions with thinner sample thickness to strain from residual load induced during FIB deposition, together with increased thermal expansion in these areas due to their higher surface-to-volume ratio. The results highlight the importance of considering sample thickness (and especially thickness variations) when analyzing the local bulk plasmon energy for temperature measurement using PEET. However, in case of W, an increasing beam broadening (FWHM) of the bulk plasmon peak with decreasing sample thickness can be used to improve the accuracy of PEET in TEM lamellae with varying sample thickness.

1. Introduction

Scanning / Transmission electron microscopy (S/TEM) has been established as a powerful method for atomic-scale material characterization [1]. The further advancement of *in-situ* capabilities to expose materials to relevant process and application conditions opens access to structure-property correlations in materials [2–4]. Particularly, the development of microelectronic mechanical systems (MEMS) as *in-situ* sample stages [5,6] enable real-time observation of material under appropriate stimuli such as heating [7,8], electric biasing [9,10], mechanical deformation [11] etc. in S/TEM experiments with a resolution up to the atomic scale [12,13].

For example, S/TEM heating experiments have been widely applied for understanding thermally induced microstructure dynamics in materials such as phase transformations in metals (e.g. [14,15]). To accurately correlate the findings from *in-situ* heating experiments to other microstructure information, e.g. to correlate results with predictions from phase-temperature or time-temperature diagrams, it is important to measure the temperature *in-situ*, accurately across the TEM sample. Thus, it is imperative to develop methods for *in-situ* temperature measurement [16,17]. In particular, this allows for precise control of a temperature profile during an *in-situ* heating experiment to introduce specific thermal conditions, e.g., introducing temporal and spatial thermal gradients [18], mimicking the non-equilibrium thermal

* Corresponding author.
E-mail address: jojin@dtu.dk (J.R. Jinschek).
[1] These authors contributed equally

https://doi.org/10.1016/j.ultramic.2025.114102
Received 29 July 2024; Received in revised form 20 December 2024; Accepted 2 January 2025
Available online 4 January 2025
0304-3991/© 2025 The Author(s). Published by Elsevier B.V. This is an open access article under the CC BY license (http://creativecommons.org/licenses/by/4.0/).

conditions as in additive manufacturing processes. Therefore, accurate local temperature measurements across the sample are required to achieve controllability of temperature settings in *in-situ* heating experiments with nanometer resolution across micrometer-sized TEM samples.

Over the years, various approaches have been developed to measure the temperature of a TEM sample [16,17]. For example, several thermometric methods utilize properties of thermometric materials, such as temperature-dependent sublimation rate of silver (Ag) particles (with a temperature accuracy of $\pm$ 5 °C) [19] or a phase transition of vanadium dioxide (VO_2) nanowires [20]. These characteristic temperature points can provide a direct binary temperature measurement. However, the application is limited by size dependencies, nano-size effects of phase transition as well as potential effects of the local environment due to residual reactive gas species in the high vacuum environment in the microscope or to reactive gas environments in *in-situ* reaction experiments. Further, electron diffraction (ED) techniques have been applied to determine temperature from shifting of Bragg peaks by thermal expansion of the material [21,22] allowing e.g. different measurement points across the reference sample of a thin Au film (with a temperature accuracy of $\pm$ 2.8 °C) [22]. The measurements of temperature-dependent changes in ED patterns require a high phase stability in materials and a critical alignment of the TEM to maintain a highly parallel beam illumination [22]. Besides, spatial resolution is strongly limited by the size of the illumination. Achieving higher spatial resolution, down to the atomic scale, is possible by switching to a focused probe and leveraging the temperature susceptivity of low angle thermal diffused scattering (TDS) as demonstrated by M. Zhu et al. [23]. Careful selection of the collection angles is crucial, as the correlation between TDS intensity and temperature exhibits multiple sign reversals. These optimal angles depend on the sample and experimental configuration but can be determined with the aid of simulations. Accurately targeting these angles with conventional scintillator-based STEM detectors presents significant challenges. In contrast, recording the full convergent beam electron diffraction (CBED) pattern using a pixelated detector offers a more straightforward approach. Nevertheless, achieving a sufficient signal-to-background ratio for the weak TDS signal relative to the intense Bragg peaks requires a pixelated detector with a high dynamic range. This requirement makes mapping via 4D-STEM acquisition data-intensive and potentially impractical for routine use by most users. Another method to measure the temperature uses the frequency shift of Raman peaks in materials in correlation with the sample temperature, however this requires a complex integration of a Raman spectrometer to measure the temperature on a sample inside a TEM [24]. The principle of detailed balance can also be applied to measure sample temperature using STEM-EELS. This principle states that the ratio between the probability of an electron exciting the sample from its initial energy state (E_1) to a higher state (E_2) and the probability of the sample de-exciting in opposite direction, giving energy to the probing electron, is given by $\exp(-(E_2 - E_1)/(k_B T))$, with k_B being Boltzmann constant and T the sample temperature. This temperature dependent ratio is retrievable from an EELS spectrum by measuring the ratio between a corresponding couple of loss and gain peaks. Idrobo et al. [25] demonstrated that the phonon loss and gain peaks measured in EELS in aloof beam mode can be used to measure the temperature of h-BN nanoflakes. In a similar way, Lagos et al. [26] showed that this method can also be applied on a MgO nanocube (as well as in direct beam mode) to measure temperature with an uncertainty of $\pm$ 1 °C. Although this method allows for a direct (calibration-free) way of probing for local temperature it requires a highly monochromated beam with an energy resolution in the meV range. Currently only a handful of instruments can provide this, making it inaccessible for most TEM users. Other studies [27] have used confocal microscopy and exploited luminescence spectra of nanoparticles to measure temperature with an accuracy of better than 4 °C for temperatures up to 250 °C (523 K). Given the photonic nature of the technique the spatial resolution is however limited to ~1 μm. Similarly, the cathodoluminescence frequency in semiconductors has been applied for temperature measurement. Here the drawback is a high sensitivity to heterogenicities in the local composition, causing an uncertainty of up to 50 °C [28].

Here in our study, we decided to investigate the accuracy of plasmon energy expansion thermometry (PEET) [29–41] as the method to measure local temperature in a S/TEM sample using STEM-EELS. PEET has been introduced in the past as a non-contact thermometric method capable of mapping local temperature profiles across a S/TEM sample with nanometer spatial resolution [38].

A bulk plasmon describes the collective oscillation of the valence electrons within the material excited by an external electric field. The main principle of PEET is therefore to exploit the temperature dependence of a material's bulk plasmon energy (E_p), expressed by:

$$E_p = \hbar\sqrt{\frac{ne^2}{m\varepsilon_0}} \tag{1}$$

according to the free-electron model, where $\hbar$ is the reduced Planck constant, ε_0 the permittivity of vacuum and n is the density of valence electrons with charge e and mass m. The temperature dependence of E_p arises from the principle of thermal expansion, which affects n [42]. Consequently, a prerequisite for PEET is that in the temperature range of interest, no phase transformation nor abrupt morphological or structural change may occur inside the sample, as this would lead to a sudden irreversible alteration of n.

Previous work on PEET has demonstrated the temperature-dependent shift in E_p in various materials such as a polycrystalline tin (Sn) film of 2.5 mm diameter [43], silicon (Si) nanoparticles [44], aluminium (Al) thin films [45] and silver (Ag) films [39] with increasing temperature. In more recent years, the focus in method development has been on pushing the spatial and temperature resolution achievable with PEET. In 2015, Mecklenburg et al. [38] mapped an inhomogeneous temperature distribution ranging from RT to 327 °C (with a thermal gradient of the order of 10^4 °C/m) across a 80 nm-thick serpentine Al wire with a length of 0.8 μm, achieving a spatial resolution of 3 nm limited by the delocalization length of Al plasmon. In a subsequent study in 2018 [37], they incorporated drop-casted Si nanoparticles of 90 nm in size to expand the applicability of PEET from RT to 1250 °C. However, the low thermal expansion of Si (zeroth-order thermal expansion coefficient of 3.3×10^{-6} °C^{-1}) led to low sensitivity to measure a temperature change. Similarly, Chmielewski et al. [36] used dry-deposited 50-nm-sized Al nanoparticles to measure the local temperature on a MEMS heating chip in vacuum and in hydrogen (H_2) environment. Shen et al. [31] studied molybdenum disulfide (MoS_2) with a large thermal expansion coefficient of 1.9×10^{-5} °C^{-1} to measure thermal gradients of 8×10^7 °C/m (temperature difference of 200 °C over 2.1 μm length). They reported a temperature precision of 20 °C achieved by averaging measured plasmon energies along a column of pixels transverse to the gradient. This temperature precision in combination with the known thermal gradient resulted in a spatial resolution of 250 nm. Barker et al. [29] reported on measurements on Si nanoparticles using an optimized and automated plasmon peak fitting scheme allowing to live-process the average temperature over a selected region of interest (ROI). By collecting sufficient statistics from a homogeneously heated ROI, they have reported sub-50 °C resolution. Lastly, just recently Kumar et al. [33] exploited PEET to measure cryogenic temperatures in cryogenic TEM holders using again Al as specimen material.

So far, PEET has been applied to measure temperature in (clusters of) nanoparticles, thin films and various two-dimensional (2D) materials, but a potential influence from sample thickness on E_p has not been systematically investigated yet. Additionally, the applicability of PEET on focused ion beam (FIB)-prepared lamellae, where thickness inhomogeneity is often encountered, remains unclear. To the best of our knowledge, there are only a few details in previous studies addressing a possible sample thickness effect on E_p. Mecklenburg et al. [38] reported

that the local thickness variation from 0.03 to 0.34 relative thickness (t/λ) (within an otherwise homogeneous 80 nm-thick Al wire) does not show a correlation with E_p. Mitome et al. on the other hand [44] states an inverse square relation of E_p to Si nanoparticle cluster sizes ranging from 3.5 nm to 10 nm. They conclude that this relation is caused by a quantum confinement effect. Similarly, Hu et al. [35] addressed the difference in thermal expansion within the different layers of 2D materials, such as graphene, MoS_2, $MoSe_2$, WS_2 and WSe_2, also because of quantum confinement effects. These last two studies suggest that E_p might be affected by the sample thickness. This is particularly expected for FIB lamellae with typical thicknesses well below 100 nm [10,18,46,47] due to potential deviation in thermal expansion compared to bulk values caused by surface effects or induced-strain effects.

The aim of this paper is to investigate further this possible dependence of E_p on sample thickness as this would have a significant effect on the accuracy of PEET, especially when applied to specimens with inhomogeneous sample thickness. Tungsten (W) was selected as the model material, because it is stable and is the metal with the highest melting point (at atmospheric pressure bulk tungsten melts at 3410 °C [48]). This choice delays temperature induced morphological changes and melting effects in the heating experiments. In addition, W is known to exhibit a sharp plasmon resonance [49–51] which leads to high signal-to-noise ratios (SNR) in E_p measurements compared to other materials and enables accurate E_p determination. A W lamella with varying thickness was prepared and STEM-EELS mapping has been exploited to measure local sample thickness (t/λ - log-ratio method) as well as corresponding local bulk E_p at different temperatures. The experimental results showed a clear correlation between specimen thickness and E_p at all set temperatures. It was found that the E_p deviates more from theoretical expected values at the thinner region. It is shown that PEET can however still be performed by using thickness-dependent thermal expansion coefficients. Finally, an alternative calibration method is proposed, where E_p and the simultaneously observed broadening of a plasmon peak are combined into a thickness-independent parameter that is, however, still temperature-dependent to retrieve the local temperature across a TEM sample with varying thickness.

2. Method

2.1. TEM sample preparation for in-situ heating experiment

A Helios 5 Hydra UX plasma focused ion beam (PFIB) DualBeam® system (Thermo Fisher Scientific Inc.) was used for the TEM sample preparation. The W lamella used for this study was lifted out from a disposed W Easylift® needle. A xenon (Xe) plasma beam at 30 kV with beam currents of initially 16 nA and then 4 nA was used in the first step of trenching, while for cross section thinning a beam current of 1 nA were used. To polish the sample to electron transparency (< 100 nm) and to minimize the thickness of the amorphous surface layer, a Xe plasma beam setting of 5 kV and 30 pA was used. During this polishing process, the sample was tilted from 3 to 7° to achieve a thickness gradient at the centre of the W lamella. After polishing, the W lamella was lifted out using the Easylift® needle. To attach the sample on the MEMS heater, W gas injection and Xe plasma beam settings of 30 kV and 0.1 nA were used. The lamella (with dimension of 5 μm by 13 μm) was positioned over a through-hole window of a Wildfire® heating chip (DENS Solutions B.V.). This chip was placed on a 45° pre-tilt stab [46]. For process examination during the lift-out process, secondary electron (SE) imaging in scanning electron microscopy (SEM) mode using the electron beam was performed at 30 kV and 30 pA.

The through-hole type Wildfire® heating chip allows heating to temperatures ranging from RT up to 1300 °C with a stated accuracy of 5 % at the centre windows [52]. This is achieved by Joule heating of a metallic heating spiral connected to a 4-point-probe sensing setup that monitors its temperature precisely by measuring its temperature-dependent resistance. A low sample drift rate down to 0.1 nm/min enables high stability and high spatial resolution during heating experiments [52]. The chip was used in combination with a dedicated Wildfire single-tilt® TEM heating holder.

2.2. EELS spectra acquisition in STEM mode

The STEM-EELS acquisitions were performed using a monochromated Titan X-FEG® (Thermo Fisher Scientific Inc.) operated at an accelerating voltage of 300 kV. The EELS maps in STEM mode were collected using a Quantum 966® Gatan Image Filter (GIF) with Dual-EELS® capability and a US1000XP® camera. The Wien-filter monochromator allowed an energy resolution of 130 meV ± 10 meV, as measured by the full-width at half maximum (FWHM) of the zero-loss peak (ZLP). All EELS measurements were performed in micro-probe mode at a beam current of approximately 0.1 nA using a semi-convergence angle α of 1.90 mrad and semi-collection angle β of 4.60 mrad. The selection of these specific α and β values was based on preliminary measurements using various combinations of α and β, aiming for optimal measurement of E_p (see details in ***SI.2)***. The details of the exact determination of α and β can be found in ***SI.1***.

2.3. Estimation of absolute sample thickness

The EELS map for thickness estimation was acquired at 20 °C over a rectangular ROI encompassing the thickness gradient of interest. The thickness in units of inelastic mean free path (t/λ) can be obtained by EELS and the log-ratio method [51,53] with formula $t/\lambda = \ln(I_t/I_0)$. Here I_t is the total transmitted intensity (including the ZLP) and I_0 is the intensity corresponding to the ZLP. In order to estimate t/λ as accurate as possible, a relatively high energy dispersion of 0.25eV/pixel was used to cover a wide range of energy loss (i.e. from - 35 eV to 477 eV).

To determine the absolute thickness value, the inelastic mean free path in W has to be estimated as well. Here the formula from [53] was used in combination with an effective semi-collection angle (β^*) to take the incident-probe convergence into account:

$$\lambda = \frac{106FE_0}{E_m \ln\left(\frac{2\beta^* E_0}{E_m}\right)} \tag{2}$$

The result is expressed in units of nanometers and $F = [1 + (E_0/1022)]/[1 + (E_0/511)]^2$ is a relativistic factor equal to 0.513 for incident electron energy E_0 of 300 keV. E_m is an average energy loss defined by $E_m \approx \int S(E)dE / \int (S(E)/E)dE$ where $S(E)$ is the single scattering distribution (the experimental spectrum with plural scattering removed). These formulas are derived from electron scattering theory and more specifically from the Kramers-Kronig sum rule [54,55]. To estimate E_m, Malis et al. [53] determined a phenomenological relation

$$E_m = 7.6Z^{0.36} \tag{3}$$

in function of atomic number Z. The calculation of the absolute thickness by the procedure described above was done using Digital Micrograph 3.20 (Gatan Inc., New York, USA) where I_0 was determined by extracting the ZLP using the reflected tail model [56] and I_t by summing the intensity from -35 eV till 477 eV. The provided parameters were $E_0 = 300$ keV, $\alpha = 1.90$ mrad, $\beta = 4.60$ mrad and Z (for W) = 74.

2.4. W bulk plasmon peak characterization in STEM-EELS

The PEET measurements were conducted at a set temperature of 20 °C (RT), then 150 °C, 200 °C, 250 °C and continuing with increments of 50 °C up to 1000 °C. A heating rate of approximately 50 °C/s was applied, with a pause of 1 min at each set temperature to ensure a stable temperature readout from the heating device before conducting the STEM-EELS experiments. The ROI for collecting the W bulk plasmon peak was chosen to include the same thickness gradient of which the

absolute thickness was mapped, as described in the previous paragraph. The STEM-EELS maps were acquired in DualEELS® mode at the dispersion of 0.01 eV/pixel. For each probe position, the first spectrum captured the ZLP in the energy range from approximately - 7.00 eV to 13.47 eV, while the second spectrum recorded the W bulk plasmon peak from 13.00 eV to 33.47 eV. These two spectra are referred to as the *ZLP spectrum* and the *plasmon spectrum*, respectively, in the remainder of the document. Besides the advantage of collecting both the ZLP and the plasmon peak at the dispersion of 0.01 eV/pixel, DualEELS® also allows recording the plasmon spectrum at a longer exposure time in order to increase SNR. The exposure times at each probe position were set to 0.002 s and 0.098 s, respectively, corresponding to a total dwell time of 0.1 s. For mapping a step size of 31 nm in x and y was chosen. For more details about ROI corrections between acquisitions see ***SI.3***.

The acquired data was processed and analysed using the python pyEELSMODEL module [57]. First the energy axis on every pair of ZLP spectrum and plasmon spectrum were aligned to set the ZLP at 0 eV of energy loss. Afterwards both the ZLP and plasmon peak were fitted in order to determine their respective peak position with sub-pixel precision. The considered fitting windows ranged from - 0.5 eV to 0.5 eV for the ZLP and from 17.5 eV to 30 eV for W plasmon peak, respectively. The trust-region-reflective least squares fitting algorithm was used. Several fitting models suggested by literature [29,36,37] were investigated on both peaks and compared based on their reduced χ^2-value maps (details are shown in the ***SI.4.1***). Based on these maps, a Voigt curve fitting was used for fitting the ZLP and a Johnson's S_U curve for fitting the plasmon peak. The Johnson's S_U curve has five parameters and can be asymmetric, this resulted in good fits at all probe positions even in cases when the plasmon peak was asymmetric (details in ***SI.4.2***). Unlike in case of the Voigt curve fitting, none of the Johnson's S_U curve parameters however represent its mode directly, so this was determined by numerically finding the root of its (analytical) derivative. To determine the E_p, the fitted mode of the plasmon peak was simply subtracted from the fitted centre of the ZLP. Finally, broadening of the plasmon peak was determined by determining its full-width half maximum (FWHM) calculating the distance between the roots of its fit subtracted by half its max value. The FWHM values have been used to monitor the broadening of the plasmon peak and thus its potential correlation with changes in sample thickness. All numerical root-finding for both determination of plasmon fit mode and FWHM were performed using 'fsolve' function from the scipy.optimize python module [58]. This function uses a modified Powell's dog leg method. The E_p maps and FWHM maps at the different set temperatures are shown in ***figure S7*** and ***figure S8*** respectively (see ***SI.4.3)***.

2.5. Determining I_t-map and relative thickness map

In addition to the E_p and FWHM maps, two more maps were derived from every DualEELS® data set at a given temperature: the total transmitted intensity (I_t) map and the relative thickness map. To generate these maps, the ZLP and plasmon spectra at each probe position were combined into a single spectrum. However, a direct combination was not feasible due to differing exposure times and, consequently, a factor of ~48 difference in dose between the two spectra. Furthermore, both spectra shared an overlapping energy range from 13.0 eV to 13.47 eV. To address this, the average ZLP and plasmon spectra were analysed in the overlapping region, where the signal was flat, allowing the determination of the exact signal ratio between the two spectra based on their mean values in this range. For each probe position, the plasmon spectrum was then scaled by this ratio, and the overlapping range was cropped in the ZLP spectrum due to its higher shot noise relative to the plasmon spectrum. At last, the pairs of ZLP and plasmon spectra were combined, and the energy axis aligned to have the ZLP's mode at 0 eV. I_t maps at different set temperatures could then be extracted allowing the monitoring of possible morphological changes with increasing temperature (***SI.5***).

Relative thickness maps were calculated using $\ln(I_t/I_0)$ where I_0 was taken as the total counts of a Voigt-fitted ZLP within an energy interval from - 3.0 eV to 3.0 eV, again using the trust-region-reflective least squares fitting algorithm. Although this formula is the one used for calculating the specimen thickness in units of inelastic mean free path (t/λ), here it is not giving accurate values as the energy range of the spectrum is limited to <33.0 eV (after alignment of ZLP). The value does however give accurate relative differences in thickness and can among others be used for monitoring integrity of the thickness profile of the lamella with increasing temperature.

Considering the constant thickness of the specimen along the vertical axis (y-axis) in the mapped ROI, the remainder of this paper primarily focuses on the averaged horizontal line profile of various maps, including absolute thickness, E_p, FWHM and t/λ maps. By averaging the signal over the 16 pixels along the y-axis at each probe position along the x-axis, statistical weight was gained, allowing for the determination of the corresponding standard error for each x-pixel. This standard error is taken as the final error for the signal at the given x-pixel, and this approach is again justified by the consistent thickness observed along y-axis. The obtained relative thickness profiles from the $\ln(I_t/I_0)$ maps allowed to determine final corrections in horizontal shift to properly align the increasing thickness for all set temperatures. Slight misalignments of 124 nm at the maximum (4 pixels × 31 nm) originate from slight mismatch in mapped region between the acquisitions at different set temperatures. The horizontal shift corrections were applied to all maps, after which they were cropped to a width of 93 pixels instead of the originally 100 pixels width. Minor vertical shifts were also noted between maps but since the thickness symmetry along y-axis extended in regions above and below the ROI this was found to be negligible.

Finally, it was verified that the average relative thickness profiles attained from the DualEELS® measurements have a linear relation to the average absolute thickness profile attained from the 0.25 eV/pixel dispersion EELS measurement. Therefore, a linear relation between the relative thickness values measured at 20 °C and absolute thickness values (also measured at 20 °C) was derived. This linear relation was then used to transform all relative thickness values at all other set temperatures to absolute thickness values. It must be noted that the obtained absolute thicknesses at temperatures higher than 20 °C are only approximately correct as thermal expansion effects are not accounted for here.

2.6. Simulations of sample temperature using finite element method (COMSOL)

To predict the potential temperature distribution in the W lamella deposited on the MEMS heating chip, finite element method (FEM) simulations were conducted using COMSOL Multiphysics® software [59]. These simulations, based on heat transfer theory in solid mechanisms, included three modules: electric current, solid mechanics, and heat transfer in solids. All relevant aspects of the physical system and interactions among the modules were simulated simultaneously, modelling from the Joule heating principle to heat transfer across the entire geometry. To mimic the vacuum environment in TEM, only radiative heat loss and heat flux from conduction were assumed in the heating simulation.

The finite element model consisted of the free-standing membrane area with the embedded heating spiral and the W lamella attached to it. To simulate the temperature distribution across the W lamella in comparison with the PEET measurements, the equilibrium state of the heating experiment was considered at each set temperature. Therefore, the simulation did not include the difference in heat transfer at the interface between the SiN membrane and the W lamella. In the PEET experiments, this effect would be detectable by the change in the electric resistance of the metallic heater, which is then compensated by the heater's working principle. Using Joule heating and the 4-point probe measurements, the temperature-dependent resistance of the metallic

heater is measured constantly, and the power of the heater is adjusted accordingly to maintain the set resistance of the metal heater, thus stabilizing the set temperature values. STEM-EELS experiments were therefore conducted after a pause of about 1 min at each set temperature to ensure measurement under such a stable temperature condition under equilibrium. The thickness of the lamella was also included into the model. A tetrahedral mesh was used with a mesh size from 0.2 μm to 10.5 μm, and mesh rate at the sample area was set to 0.2. The thermal properties of W were taken from the COMSOL library with the coefficient of thermal expansion (CTE) of 4.5 × 10^{-6} °C^{-1}, thermal conductivity of 175 W/(m × K) and the emissivity of 0.361. Due to the polycrystalline cubic structure of the W sample, an isotropic thermal conductivity is assumed in simulation. The electric voltage was ramped from 0.746 V to 1.421 V in correlation with the set temperatures ranging from 300 °C to 1000 °C (shown in figure ***S8b***), with the set temperature defined by the temperature at the centre of the MEMS heating spiral. In order to evaluate the accuracy of our simulations, a separate model was made consisting of just the free-standing membrane area with the embedded heating spiral without lamella. Simulations of this model at different set temperatures showed good agreement with the values reported by van Omme et al. [52] (more details in ***SI.6)***.

3. Results

Fig. 1a shows a SEM image of the heating spiral of the MEMS heater using secondary electrons (SE), and the higher magnification SE image in Fig. 1b shows the W lamella deposited over the through-hole window of the MEMS heater. The ROI around the thickness gradient that got mapped during the heating experiments is indicated by a dashed rectangle in Fig. 1b. Its absolute thickness map is displayed in Fig. 1c. This map was derived from an EELS dataset acquired at 20 °C (prior to heating) with an energy dispersion of 0.25 eV/pixel, as previously described. The line thickness profile shown in Fig. 1d indicates varying thickness between approximately 30 nm and 70 nm which is the range of thicknesses present in most FIB-prepared electron-transparent TEM samples [46,47,60,61]. As stated earlier in the methods, the error bars for the values are standard errors from averaging every column along the vertical y-axis transient to the thickness gradient.

The results from the FEM simulations are shown in Fig. 2. As an example, for a set temperature of 700 °C at the centre of the spiral, the temperature distribution over the entire geometry is shown in Fig. 2a. Zooming in at the W lamella (Fig. 2b) the temperature reaches between 690 °C and 700 °C. Such deviations in temperature between setpoint and sample area of up to 5 % are within the accuracy of the vendor calibration [52] and have been reported before in actual heating experiments [18]. The considered thickness profile along the double-arrowed line in Fig. 2b is shown in Fig. 2c, resembling the measured thickness profile of the actual sample as depicted earlier in Fig. 1d. Temperature line profiles along the double-arrowed line show homogeneous temperature across the W lamella for all set temperatures from 300 °C to 1000 °C (with step of 100 °C). These FEM simulations indicate that temperature should be independent of the specimen thickness variations between 30 nm and 70 nm. As mentioned above, the deviation between the simulated temperature over the W lamella and the setpoints from 300 °C to 1000 °C are all within the accuracy of 5 %.

As explained in the *Methods* section, the DualEELS® measurements for the study of E_p were performed on the same ROI as in the absolute thickness map of Fig. 1c for temperatures ranging from 20 °C to 1000 °C. The resulting E_p and plasmon FWHM maps are shown in figures ***S6*** and ***S7***, respectively. Due to noted morphological change in the I_t maps at temperatures above 750 °C (see ***SI.5***), only data at set temperatures ranging from 20 °C to 700 °C are included from now on (not limiting the main focus of our study), as morphological or structural changes are irreversible and limit the applicability of PEET (see *Introduction*). This observed morphological change is most likely due to recrystallization starting at this temperature in the thinnest part of the W lamella (for further discussion see the details in ***SI.5***).

Maps of E_p and FWHM are shown in Fig. 3 for selected set temperatures of 20 °C, 500 °C and 700 °C, respectively. Fig. 3a indicates two important trends. First, a red shift in the E_p maps is observed with increasing temperature, as expected from the principle of PEET. The average E_p value shifts from 25.35 eV ± 0.16 eV to 25.18 eV ± 0.13 eV with increasing temperature from 20 °C to 700 °C. The error of 0.16 eV and 0.13 eV here are calculated standard deviations. Secondly, a thickness dependence is evident, shown by a change in E_p (visible as a colour change to green/yellow in the E_p maps in Fig. 3a) around the thinnest part of the sample of approximately 30 nm (see Fig. 1c). Even though a clear thickness dependence of E_p is seen, it can be noted that the measured average E_p, especially at 20 °C, is in good agreement with earlier literature values of 25.3 eV [62,63] and 25.5 eV [64,65] reported for unspecified thickness and temperature condition.

Upon comparing to the corresponding thickness profile in Fig. 1d, it becomes more evident that E_p decreases with increasing thickness from the approximated 30 nm to 70 nm. At 20 °C, E_p decreases by 0.427 eV ± 0.009 eV from 25.632 eV ± 0.008 eV to 25.204 eV ± 0.004 eV. At 500 °C, E_p decreases by 0.400 eV ± 0.009 eV from 25.508 eV ± 0.008 eV to 25.108 eV± 0.004 eV. At 700 °C, E_p decreases more significantly by 0.306 eV ± 0.009 eV from 25.381 eV ± 0.008 eV to 25.075 eV ± 0.004 eV. The FWHM maps in Fig. 3b show a thickness dependency at 20 °C, 500 °C and 700 °C, with a larger FWHM value at the thinnest region. At 20 °C, the FWHM increases from 7.67 eV ± 0.02 eV (at 60 to 70 nm thickness) to 11.65 eV ± 0.10 eV (at 30 to 40 nm thickness), at 500 °C from 7.85 eV ± 0.03 eV to 11.25 eV ± 0.10 eV and at 700 °C from 7.90 eV ± 0.02 eV to 11.31 eV ± 0.10 eV, respectively.

To quantitatively analyse the relationship of E_p and FWHM with sample thickness, values were extracted from their maps (Fig. 3a and 3b

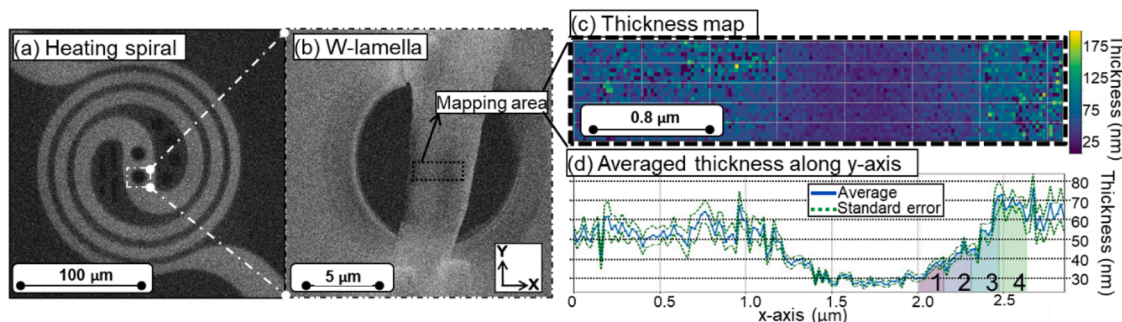

Fig. 1. Experimental setup of the TEM heating experiments and the absolute thickness map of the W-lamella. (a): SEM SE image of the MEMS heating spiral and (b) of the W-lamella placed over the central window in the magnified area in (a). (c): The absolute thickness map corresponding to the assigned area in (b). (d): Line profile of (c) along x-axis showing the average (along y-axis) thickness variation of the W lamella with standard error. Four different thickness regions are indicated in (d) by a colour code with numbers 1 to 4.

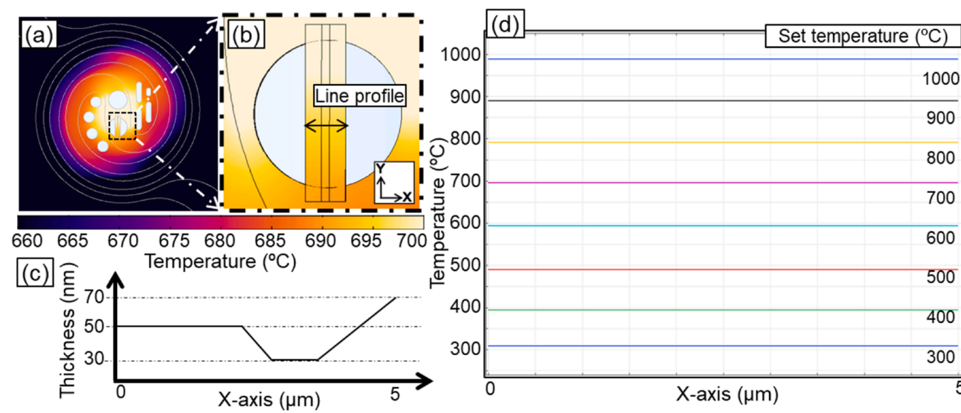

Fig. 2. FEM simulations of the temperature distribution of the heating chip with the W lamella (a): Entire geometry of the model including free-standing membrane with embedded heating spiral and W lamella with varying thickness. (b): Attached W lamella over the magnified area indicated in (a). (c): Schematic diagram of the considered line thickness profile of the sample geometry along the double-arrow line in (b). (d): Line temperature profiles along the double-arrow line in (b) at set temperatures from 300 °C to 1000 °C with steps of 100 °C.

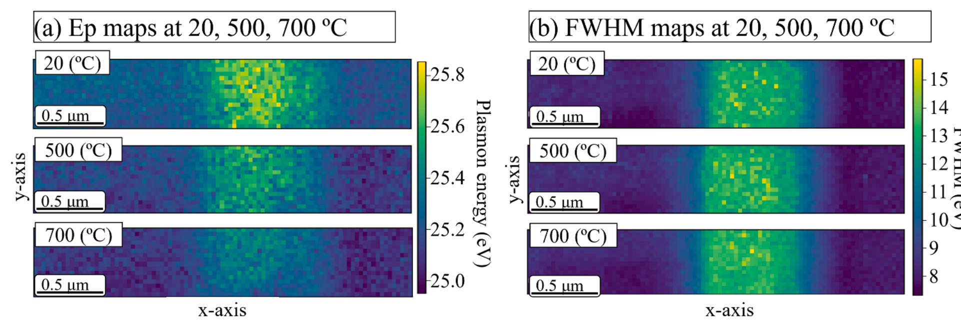

Fig. 3. Maps of measured W E_p (a) and FWHM (b) over the W lamella with varying thickness at set temperature of 20 °C, 500 °C and 700 °C. The mapped area is the same as in *Fig. 1c*. Pixel size is 0,02 µm x 0,02 µm.

respectively) within the four selected sample thickness intervals, shown at the thickness gradient area in Fig. 1d. The thickness intervals range approximately from 30 to 40 nm, 40 to 50 nm, 50 to 60 nm and 60 to 70 nm, indicated by four colours (and numbered from 1 to 4). Each dataset contains 80 values with 16 pixels in y-direction (width of 0.48 µm) and a 5-pixel interval along x-axis (length of 0.15 µm). Fig. 4a shows the average values of E_p within each of these distinct thickness ranges, when ramping the set temperature from 20 °C to 700 °C. As highlighted earlier, E_p shows a decreasing trend with an increase in sample temperature as well as a decrease in average E_p with increasing sample thickness. In addition, Fig. 4a clearly indicates a more pronounced decrease in E_p with increasing temperature for thinner sample areas.

Fig. 4b displays the average FWHM of the W bulk plasmon peak at each thickness region at set temperatures from 20 °C to 700 °C. It shows that the FWHM does not vary significantly with temperature but increases with thickness. The shown error bars in Fig. 4a and 4b are calculated standard errors. Since the thickness within the intervals varies approximately linearly along the x-axis rather than remaining constant, these error bars represent an upper bound on the uncertainty.

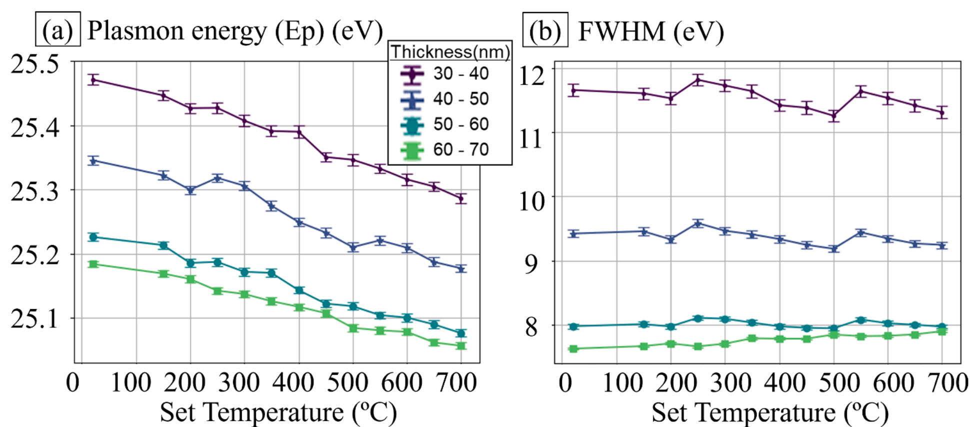

Fig. 4. Average E_p (a) and FWHM (b) of the plasmon peak in function of set temperatures from 20 °C to 700 °C for different thickness regions ranging from 30 to 70 nm. The error bars correspond to the standard error. Legend shared between (a) and (b) shows the corresponding thickness regions, which are extracted from the absolute thickness map, in Fig. 1d with assigned colour blocks and numbers.

4. Discussion

The results show a clear thickness dependence of E_p of W at the different set temperatures. This dependence affects the accuracy of the conventional PEET method which does not take thickness variations into account. In the following, this influence will be evaluated in more detail and approaches to take it into account are proposed.

4.1. Temperature-dependence of E_p of W - theory and experiments

- *Expected temperature-dependence of E_p of W - based on theory*

As mentioned in the *Introduction*, the common procedure of PEET is based on the free-electron model (eq. (1)) to derive temperature from E_p trough the temperature-dependant valence electron density *n(T). n(T)* can be expressed in terms of the coefficient of linear thermal expansion (CTE, α_l) as:

$$n(T) = n(T_0)\cdot\left[1 - 3\left(\int_{T_0}^{T}\alpha_l(T')\cdot dT'\right)\right] \quad (4)$$

where $n(T_0)$ is the density of valence electrons at an initial temperature T_0 and $n(T)$ is the density of valence electrons at temperature T. Combining eqs.1 and 4, the temperature-dependent E_p can be expressed as:

$$E_p(T) = E_p(T_0)\cdot\left[1 - \frac{3}{2}\left(\int_{T_0}^{T}\alpha_l(T')\cdot dT'\right)\right] = E_p(T_0)\cdot\left[1 - \frac{3}{2}\cdot\alpha_0\cdot\Delta T\right] \quad (5)$$

where α_l was expanded till zeroth order. Accordingly, the temperature-dependent shift in E_p can be calculated using values of the initial plasmon energy ($E_p(T_0)$) and the zeroth-order CTE (α_0):

$$\frac{\Delta E_p}{\Delta T} = -\frac{3}{2}\cdot E_p(T_0)\cdot\alpha_0 \quad (6)$$

where ΔE_p is $E_p(T) - E_p(T_0)$ and ΔT is $T - T_0$.

For comparison: in case of aluminium (Al) as used by Mecklenburg et al. [38] with a bulk E_p at RT of E_p (T_0) = 15.8 eV and a zeroth-order CTE of $\alpha_0 = 23.5\cdot10^{-6}$ °C^{-1}, the shift in E_p for a 1 °C change in temperature is approximately 0.557 meV. For the W, as considered here, the literature value for α_0 is $4.31\cdot10^{-6}$ °C^{-1} ± $0.01\cdot10^{-6}$ °C^{-1} [66] and the average measured E_p is 25.35 eV ± 0.16 eV (standard deviation as error) at 20 °C (Fig. 3a). The E_p shift per 1 °C is expected to be around 0.164 meV ± 0.02 meV. As a reminder: W was chosen because of the much higher melting temperature compared to Al, expanding the applicability of PEET to higher set temperatures. (*Note: The estimation of the CTE value depends on the used measurements to determine the lattice constant* [67]. *Accordingly, the error* bar *is assumed to be* <0.001 Å *for a lattice constant of* W *of 3.164* Å, *and, therefore, the error for CTE can be neglected.*)

- *Temperature-dependence of E_p of* W *– based on our results*

If the measured thickness variations (see Fig. 1) are neglected and the average E_p values from the maps shown in Fig. 3a are used to estimate the average temperature dependence of E_p, then the average E_p decreases from the earlier stated 25.35 eV ± 0.16 eV at 20 °C to 25.18 eV ± 0.13 eV at 700 °C. This corresponds to an energy shift with temperature of 0.25 meV/°C ± 0.31 meV/°C, being 1.5 times larger than the above-estimated value of 0.164 meV/°C ± 0.02 meV/°C. This already illustrates how large the influence of thickness variations can be on the accuracy of PEET if thickness is not taken into account.

- *Temperature-dependence of E_p of* W *with thickness consideration*

The relation between the induced systematic error on the measured temperature, using the free-electron model with literature values for α_0 [66], and the sample thickness was further investigated by again considering the four thickness intervals indicated in Fig. 1d.

The results are shown in Fig. 5a, where the measured temperature is plotted against the set temperature. The measured temperature at the thickest region (60 to 70 nm) is in good agreement with the set temperature within the expected 5 % uncertainty [52]. With decreasing sample thickness, the deviation between measured and set temperature increases. At a thickness of 30 to 40 nm, the deviations are approximately 214 °C and 317 °C at set temperatures of 500 °C and 700 °C, respectively. The larger deviation in the thinner area implies the thermal expansion varies with sample thickness. The zeroth-order coefficients were extracted for the different thickness regions using linear regression between ΔE_p and ΔT, as shown in Fig. 5b. The slope is seen to be more negative at smaller sample thickness, i.e. from -0.259 meV/°C ± 0.006 meV/°C in the thickness region of 30 to 40 nm compared to -0.186 meV/°C ± 0.004 meV/°C in the thickness region of 60 to 70 nm, which is the closest to the earlier mentioned theoretical value of 0.164 meV/°C. Accordingly, the deduced α_0 has a larger value in the thinner area, from 6.78×10^{-6} °C^{-1} ± 0.15×10^{-6} °C^{-1} at the thickness of 30 to 40 nm, 6.34 × 10^{-6} °C^{-1} ± 0.23×10^{-6} °C^{-1} (40 to 50 nm), 5.73×10^{-6} °C^{-1} ± 0.14 × 10^{-6} °C^{-1} (50 to 60 nm) to 4.927×10^{-6} °C^{-1} ± 0.099×10^{-6} °C^{-1} (60 to 70 nm), respectively. Compared to the literature value of α_0 of 4.31 × 10^{-6} °C^{-1} [66], the deviation becomes again larger with decreasing sample thickness.

In addition to comparing the temperature dependence of E_p and extracting α_0 in different thickness ranges, the temperature resolution was also calculated by propagating the error of α_0, $E_p(T)$ and $E_p(T_0)$ using eq. (4). The highest uncertainties found were 49 °C, 48 °C, 43 °C and 41 °C for the respective thickness ranges of 30 to 40 nm, 40 to 50 nm, 50 to 60 nm and 60 to 70 nm. These can be considered as the corresponding errors.

4.2. Estimation of the effect of sample thickness on W bulk E_p and its FWHM

To further investigate the effects of sample thickness on the W bulk plasmon peak in EELS, the values of E_p and the peak's FWHM were sorted in bins of corresponding absolute thickness. For every bin the values were averaged, and the corresponding standard errors were determined. The plots in Fig. 6 show E_p vs absolute thickness and FWHM vs absolute thickness. The absolute thicknesses are approximated values and were retrieved by calibrating the relative thickness maps as explained in the *Method* section.

- ***Effect of sample thickness on bulk plasmon energy (E_p)***

Fig. 6a shows that the E_p first increases with increasing thickness for all temperatures in the region with a sample thickness below approximately 30 nm. Afterwards, E_p starts drastically decreasing up to a thickness of 40 nm. In the sample thickness range from above 40 nm to approximately 60 nm, the decrease in E_p is less drastic with increasing thickness. Overall, the decreasing part can be approximated as decreasing by ~ 1/(absolute thickness). As outlined before in Figs. 3 and 4, the E_p is seen to increase with decreasing sample thickness and decreases with increasing set temperature. Moreover, the rate of change of E_p with temperature is again seen to be inversely proportional to thickness.

Previous reports indicate that interband transition can potentially also contribute to the shift in E_p [64,68]. However, in our study, there is no pronounced peak present in EELS in the energy region of 20.5 eV to 28.5 eV that would indicate any presence of interband transitions.

In our view, the observed thickness dependence of E_p can be explained by two aspects. First, for a given induced load, there is a higher susceptibility to strain in thin regions compared to thicker

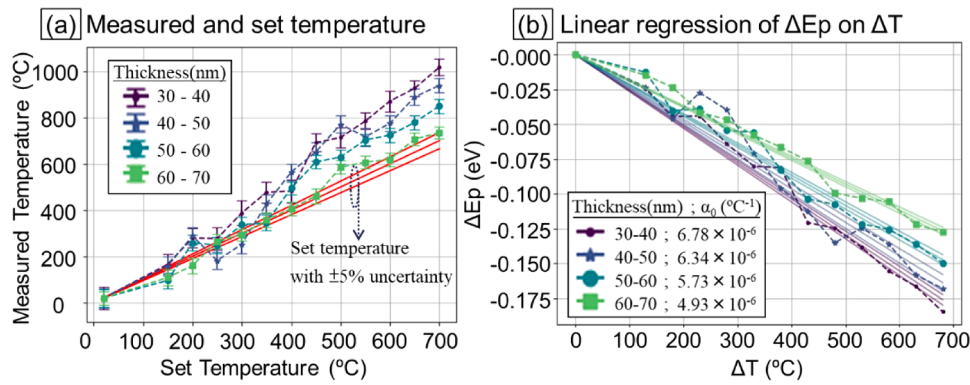

Fig. 5. (a): Measured temperature vs set temperature, according to the free-electron model using the literature value for the zeroth-order linear expansion coefficient (α_0) of W, for the different thickness regions highlighted in Fig. 1d. (b): Linear regression of ΔE_p on ΔT and extracted α_0 values for the different thickness regions considered. For every thickness interval three straight lines are present. The central line is the linear regression line and the other two represent upper and lower limit.

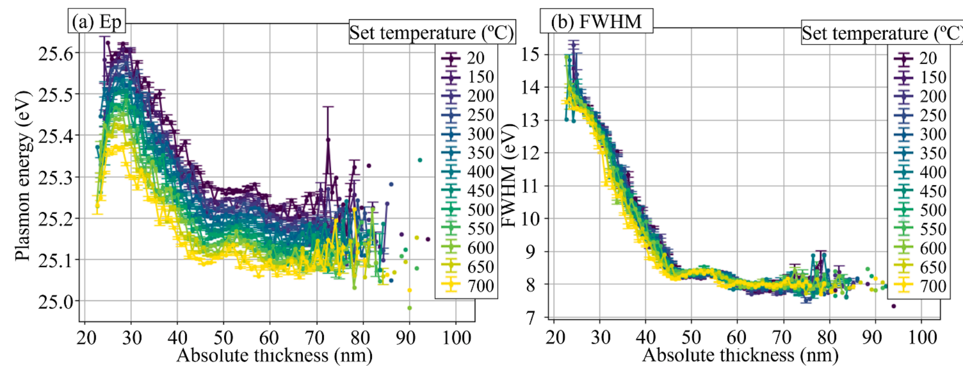

Fig. 6. Approximated absolute thickness vs (a) E_p and (b) FWHM at set temperatures ranging from 20 °C to 700 °C as shown in the legend.

regions. Strain leads to a change in density and hence a change in E_p. The strain on the lamella is presumably due to a complex residual stress induced during the FIB deposition on the MEMS heater. Furthermore, the difference in thermal expansion of the heater and the lamella adds further stress. Thermal stress simulations were performed (see ***SI.7***) and confirmed that the thinner parts of the lamella experience the largest thermal stress. However, the residual stress from the deposition is believed to have a significantly larger influence, since even before any heating (at 20 °C) a significant increase in E_p with decreasing thickness is already visible. This argument explains the thickness dependence of E_p at fixed temperatures and is consistent with previous work [69] that raised the concern that E_p is very sensitive to induced strain on thin films of aluminium nitride (AlN). Similarly, other studies have claimed that the change in thermal expansion of thin films occurred due to residual stress caused by the lattice mismatch between the film and the substrate [70,71]. This is not the case here (since no substrate was present), but it is another example of how E_p may be affected by induced stresses. The datapoint for thicknesses below 27 nm, showing an increase of E_p with thickness, comes from the edges in the thinnest part of the lamella, i.e. near $x = 1.6$ μm and 2.0 μm in Fig. 1d. Their discordant trend remains unexplained but is most likely due to a difference in the type of stress. For a better understanding, more sophisticated simulations would be required taking into account the exact geometry of the lamella and the residual load from the deposition. Secondly, the difference in rate of change of E_p with temperature at different thickness is explained by an increased thermal expansion at the thin regions due to a higher surface-to-volume ratio. This is a well-known phenomenon in nanoscale materials [70–72].

Our reasoning applies primarily to FIB-prepared lamellae and thin films, as this type of samples face the challenge of being positioned over a hole in the heater without inducing residual stress. Ideally, they are suspended freestanding to prevent induced residual stress as well as any further induced stress during heating. However, FIB-prepared lamellae are usually anchored (welded) at both ends onto the heater's surface to ensure proper thermal conduction and to prevent sample bending upon heating, which can occur when attached on one side only.

For other materials systems and sample geometry this situation might be different. Nanoparticles, for instance, are usually drop-casted onto a heater resulting in some freestanding nanoparticles on the heater's windows, where they can be heated homogeneously without displacement. This method reduces the likelihood of significant levels of stress. However, it is crucial to consider the appropriate expansion coefficient for the given size of nanoparticles to obtain accurate PEET results.

Regarding reproducibility, it should be noted that achieving identical plasmon energies in equally thick regions across different lamellae is unlikely. This is because the exact stress distribution is highly sensitive to the precise geometry of the lamella, its configuration on the heater, and the residual load introduced during deposition - all of which are challenging to control and replicate. Nevertheless, the same underlying principles are expected to apply and cause significant deviation in E_p between thick and thin regions around the given scale.

4.3. Effect of sample thickness on plasmon peak broadening (FWHM)

In addition to the value in E_p, the broadening (FWHM) of W bulk plasmon EELS peak also varies with local thickness, as shown in Fig. 3b, while being temperature independent, as shown in Figs. 4b and 6b. In the thickness range from approximately 30 nm to 60 nm, the average plasmon FWHM decreases and then saturates at higher sample

thickness. An approximate decrease of $\sim 1/(\text{absolute thickness})$ is observed, just as for E_p in Fig. 6a. Moreover, the FWHM curve corresponds very well to the E_p curve, except for the onset at the smallest sample thickness (from 20 to 30 nm). The observed E_p peak broadening shows an asymmetric enhancement on the lower-energy side of the bulk plasmon peak, as shown in the top 4 spectra in figure ***S5***, compared to the spectra in thicker regions in the bottom 4 spectra in figure ***S5***. This asymmetric broadening is the reason for the steady increase of the FWHM with decreasing sample thickness. We believe that this can be attributed to the existence of a W surface plasmon positioned at 21 eV [65]. Noteworthy is the proximity of the W surface plasmon peak at 21 eV and the bulk plasmon peak at 25 eV in our low-loss EELS signal. Hence, this finding suggests that, as the sample's thickness decreases, the influence of the surface plasmon could become increasingly pronounced. However, despite the proximity of the surface plasmon peak at 21 eV, there is no large deviation in the E_p value determined by curve fitting for two reasons. One point is that with peak broadening, the bulk plasmon still remains dominant in the spectra, as indicated in figure ***S5***, causing only neglectable changes in peak position. The other reason is that the Johnson's Su equation includes a potential asymmetry in the plasmon peak, and this reduces the effect of any deviation from a symmetrical peak shape. As shown in figure ***S4a***, the high fitting quality with low reduced $\chi 2$ values does not vary with local thickness variation (i.e. with variations in FWHM).

4.4. Delocalization length dominates spatial resolution

To minimize beam effects in the STEM-EELS experiments by minimizing STEM spot overlap during scanning, a larger pixel size of 30 nm/pixel was chosen for acquiring all EELS maps. Furthermore, we calculated the electron beam-induced heating to be <0.02 °C (as detailed in ***SI.8***), a value well below the temperature resolution and thus negligible. With an estimated sample drift of <0.1 nm/min [52] and a collection time for a map of 160 s, the maximum spot drift can be estimated as <0.3 nm, thus can be neglected here as well. To further evaluate the spatial resolution in PEET, we compared pixel size of 30 nm to the operated beam size and the localization of the EELS signal. First, the spatial resolution in Cs-corrected and mono-chromated STEM-EELS is defined by the probe size [73]. Since we applied the micro-probe STEM mode for EELS data collection with a low α of 1.9 mrad, the diffraction-limited probe size is ~ 1.26 nm. On the other hand, the localization of the EELS signal can be expressed approximately by [51]:

$$L = 0.52 \cdot \lambda / {\theta_E}^{3/4} = 2.4\ nm \tag{7}$$

where $\lambda = 1.96$pm is the electron wavelength at 300 kV and $\theta_E = 0.04$ mrad is the characteristic scattering angle for W plasmon peak at around 25.35 eV. When comparing all the length values, the pixel size of 30 nm for collecting EELS maps emerges as the primary limitation in our experiments [38], and fundamentally nanometer resolution should be possible in PEET.

4.5. Criteria for an optimal sample thickness to perform PEET on tungsten

Based on the principle of PEET, bulk plasmon energy shifts with temperature due to thermal expansion in 'bulk' materials. The point has been verified by the indications in our experiments: the E_p value 'saturates' when the sample thickness is larger than approximately 60 nm in Fig. 6a, and there is a match of the measured sample temperature with the set temperature of the heating chip at sample thickness range of 60 to 70 nm in Fig. 5b. This implies that when applying PEET, the particular material, i.e. the TEM sample, has a minimum threshold sample thickness. As an indication from our results, when using PEET to measure the temperature in W, the sample should have a homogeneous thickness distribution with a thickness larger than a determined minimum threshold value (e.g. 60 nm for W), or the sample thickness effect should be corrected.

Here an attempt is made to remove the thickness dependency of E_p by introducing a parameter ξ that depends only on temperature. This was achieved with input of the E_p that is temperature- and thickness-dependent and the FWHM that is only thickness-dependent, as shown in Fig. 7. This new parameter ξ is defined by:

$$\xi = \frac{E_p}{\frac{FWHM}{12} + 25.35\ eV} \tag{8}$$

As it can be seen in Fig. 7, the parameter ξ is thickness-independent except for the very low sample thicknesses below 30 nm. The deviation at thicknesses below 30 nm could be explained by the poor correlation between the E_p and FWHM curve shapes at this thickness region, as shown in Fig. 6. Further investigations on the parameter ξ, including a more detailed analysis of the FWHM-dependent correction of E_p, require further studies.

To optimize the application of PEET for temperature measurements of W lamellae, these considerations must be taken into account, since TEM lamellae typically have thicknesses in the range of a few 10s of nm. This most likely also applies for other materials. Accordingly, observed broadenings of the bulk plasmon peak will indicate increasing influences of the TEM sample surfaces, and the saturation region has the same thickness range as E_p, shown in Fig. 6. The deviation in values of E_p at thinner sample area could be 'mis-interpreted' as an indication of a higher local sample temperature, as indicated in Fig. 5a.

5. Conclusion

Plasmon energy expansion thermometry, PEET, has been applied to measure local temperature variations in a PFIB-prepared W TEM lamella (with a sample thickness of < 100 nm) that exhibits typical TEM sample thickness variations, including a thickness gradient from approximately 30 nm to 70 nm. This W lamella has been used to explore the effect of such a thickness non-uniformity on the bulk plasmon energy measured in EELS, which serve as the temperature-dependent measure in PEET, and on the corresponding peak broadening (FWHM). The accuracy and uncertainty in temperature measurements using PEET has been further evaluated in *in-situ* S/TEM heating experiments with chosen set temperatures between 20 °C (RT) and 700 °C.

Based on our findings and discussions, the following conclusions can be drawn when applying PEET on a W TEM lamella:

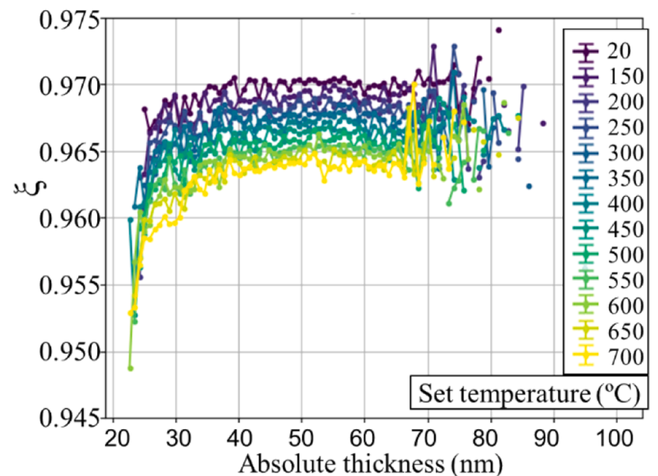

Fig. 7. The empirical value ξ from E_p and FWHM with thickness. Below the approximated 30 nm, ξ remains deviating with thickness dependence. Above this 30 nm, the ξ shows only temperature dependence as aimed for.

- For a measurement of a local sample temperature using conventional PEET, the TEM sample thickness has to be larger than approximately 60 nm in case of W.
- The achievable temperature resolution can be in the range of ± 30 °C.
- The value of the bulk E_p and peak broadening (FWHM) of the W plasmon peak are highly thickness dependent at sample thicknesses below 60 nm due to the increasing influence of strain from residual stresses induced during FIB-deposition as well as difference in thermal expansion related to surface-to-volume ratio.
- At lower sample thicknesses, the measured peak broadening of the W bulk plasmon peak has been used to correct for such thickness effects by introducing a parameter ξ.

Data availability

The data that support the findings of this study are available from the corresponding author upon reasonable request.

CRediT authorship contribution statement

Yi-Chieh Yang: Writing – review & editing, Writing – original draft, Visualization, Investigation, Formal analysis, Data curation, Conceptualization. **Luca Serafini:** Writing – review & editing, Software, Methodology, Formal analysis. **Nicolas Gauquelin:** Writing – review & editing, Investigation, Formal analysis. **Johan Verbeeck:** Writing – review & editing, Supervision, Methodology, Funding acquisition. **Joerg R. Jinschek:** Writing – review & editing, Writing – original draft, Supervision, Project administration, Methodology, Funding acquisition, Conceptualization.

Declaration of competing interest

The authors declare that they have no known competing financial interests or personal relationships that could have appeared to influence the work reported in this paper.

Acknowledgement

All authors acknowledge continued support by their colleagues at DTU Nanolab, EMAT, and NANOlab Center of Excellence. Y.-C. Y. would especially thank Murat Nulati Yesibolati for his support of the COMSOL simulations and Shima Kadkhodazadeh for fruitful discussions about the application of STEM-EELS. L.S. thanks Daen Jannis for his help with the use of pyEELSMODEL for the data processing. J.J. thanks DTU Nanolab for financial support (start-up grant). J.V. and L.S. acknowledge the eBEAM project which is supported by the European Union's Horizon 2020 research and innovation programme FETPROACT-EIC-07–2020: emerging paradigms and communities, under grant agreement No 101017720 (FET-Proactive EBEAM).

Supplementary materials

Supplementary material associated with this article can be found, in the online version, at doi:10.1016/j.ultramic.2025.114102.

Data availability

Data will be made available on request.

References

[1] D.A. Muller, Structure and bonding at the atomic scale by scanning transmission electron microscopy, Nat. Mater. 8 (2009) 263–270, https://doi.org/10.1038/nmat2380.

[2] S. Hwang, X. Chen, G. Zhou, D. Su, Situ transmission electron microscopy on energy-related catalysis, Adv. Energy Mater. 10 (2020), https://doi.org/10.1002/aenm.201902105.

[3] E. Tyukalova, J. Vimal Vas, R. Ignatans, A.D. Mueller, R. Medwal, M. Imamura, H. Asada, Y. Fukuma, R.S. Rawat, V. Tileli, M. Duchamp, Challenges and applications to *Operando* and *In Situ* TEM imaging and spectroscopic capabilities in a cryogenic temperature range, Acc. Chem. Res. 54 (2021) 3125–3135, https://doi.org/10.1021/acs.accounts.1c00078.

[4] B. He, Y. Zhang, X. Liu, L. Chen, In-situ transmission electron microscope techniques for heterogeneous catalysis, ChemCatChem. 12 (2020) 1853–1872, https://doi.org/10.1002/cctc.201902285.

[5] H. Zheng, Y.S. Meng, Y. Zhu, Frontiers of in situ electron microscopy, MRS Bull 40 (2015) 12–18, https://doi.org/10.1557/mrs.2014.305.

[6] J.R. Jinschek, Achieve atomic resolution in in situ S/TEM experiments to examine complex interface structures in nanomaterials, Curr. Opin. Solid. State Mater. Sci. 21 (2017) 77–91, https://doi.org/10.1016/j.cossms.2016.05.010.

[7] A. Kryshtal, M. Mielczarek, J. Pawlak, Effect of electron beam irradiation on the temperature of single AuGe nanoparticles in a TEM, Ultramicroscopy. 233 (2022) 113459, https://doi.org/10.1016/j.ultramic.2021.113459.

[8] R. Krisper, J. Lammer, Y. Pivak, E. Fisslthaler, W. Grogger, The performance of EDXS at elevated sample temperatures using a MEMS-based in situ TEM heating system, Ultramicroscopy. 234 (2022) 113461, https://doi.org/10.1016/j.ultramic.2021.113461.

[9] H.H.P. Garza, Y. Pivak, L.M. Luna, J.T. van Omme, R.G. Spruit, M. Sholkina, M. Pen, Q. Xu, MEMS-based sample carriers for simultaneous heating and biasing experiments: a platform for in-situ TEM analysis, in: 2017 19th International Conference on Solid-State Sensors, Actuators and Microsystems (TRANSDUCERS), IEEE, 2017, pp. 2155–2158, https://doi.org/10.1109/TRANSDUCERS.2017.7994502.

[10] O. Recalde-Benitez, Y. Pivak, T. Jiang, R. Winkler, A. Zintler, E. Adabifiroozjaei, P. Komissinskiy, L. Alff, W.A. Hubbard, H.H. Perez-Garza, L. Molina-Luna, Weld-free mounting of lamellae for electrical biasing operando TEM, Ultramicroscopy. 260 (2024) 113939, https://doi.org/10.1016/j.ultramic.2024.113939.

[11] T. Ishida, Y. Nakajima, K. Kakushima, M. Mita, H. Toshiyoshi, H. Fujita, Design and fabrication of MEMS-controlled probes for studying the nano-interface under in situ TEM observation, J. Micromech. Microengineer. 20 (2010) 075011, https://doi.org/10.1088/0960-1317/20/7/075011.

[12] A.B. Yankovich, B. Berkels, W. Dahmen, P. Binev, S.I. Sanchez, S.A. Bradley, A. Li, I. Szlufarska, P.M. Voyles, Picometre-precision analysis of scanning transmission electron microscopy images of platinum nanocatalysts, Nat. Commun. 5 (1 5) (2014) 1–7, https://doi.org/10.1038/ncomms5155, 2014.

[13] H. Wang, P.-C. Wu, Q. Zhang, X. Er, L. Gu, F. Wan, Y.-H. Chu, Q. Zhan, Atomic heterointerfaces in La0.7Sr0.3MnO3/SrIrO3 superlattices, Mater. Charact. 169 (2020) 110597, https://doi.org/10.1016/j.matchar.2020.110597.

[14] X. Liu, T.H. Man, J. Yin, X. Lu, S.Q. Guo, T. Ohmura, D.H. Ping, In situ heating TEM observations on carbide formation and α-Fe recrystallization in twinned martensite, Sci. Rep. 8 (2018) 14454, https://doi.org/10.1038/s41598-018-32896-z.

[15] Y. Song, J. Cui, L. Rong, In situ heating TEM observations of a novel microstructure evolution in a low carbon martensitic stainless steel, Mater. Chem. Phys. 165 (2015) 103–107, https://doi.org/10.1016/j.matchemphys.2015.09.001.

[16] R. Qian, X. Gong, H. Xue, W. Lu, L. Zhu, Z. An, Developments on thermometric techniques in probing micro- and nano-heat, ES Energy Environ. (2019), https://doi.org/10.30919/esee8c369.

[17] F. Gaulandris, S.B. Simonsen, J.B. Wagner, K. Mølhave, S. Muto, L.T. Kuhn, Methods for calibration of specimen temperature during *in situ* transmission electron microscopy experiments, Microsc. Microanal. 26 (2020) 3–17, https://doi.org/10.1017/S1431927619015344.

[18] S. Vijayan, R. Wang, Z. Kong, J.R. Jinschek, Quantification of extreme thermal gradients during in situ transmission electron microscope heating experiments, Microsc. Res. Tech. 85 (2022) 1527–1537, https://doi.org/10.1002/jemt.24015.

[19] S. Vijayan, M. Aindow, Temperature calibration of TEM specimen heating holders by isothermal sublimation of silver nanocubes, Ultramicroscopy. 196 (2019) 142–153, https://doi.org/10.1016/j.ultramic.2018.10.011.

[20] H. Guo, M.I. Khan, C. Cheng, W. Fan, C. Dames, J. Wu, A.M. Minor, Vanadium dioxide nanowire-based microthermometer for quantitative evaluation of electron beam heating, Nat. Commun. 5 (2014) 4986, https://doi.org/10.1038/ncomms5986.

[21] J.P. Winterstein, P.A. Lin, R. Sharma, Temperature calibration for *in situ* environmental transmission electron microscopy experiments, Microsc. Microanal. 21 (2015) 1622–1628, https://doi.org/10.1017/S1431927615015196.

[22] F. Niekiel, S.M. Kraschewski, J. Müller, B. Butz, E. Spiecker, Local temperature measurement in TEM by parallel beam electron diffraction, Ultramicroscopy. 176 (2017) 161–169, https://doi.org/10.1016/j.ultramic.2016.11.028.

[23] M. Zhu, J. Hwang, Scattering angle dependence of temperature susceptivity of electron scattering in scanning transmission electron microscopy, Ultramicroscopy. 232 (2022) 113419, https://doi.org/10.1016/j.ultramic.2021.113419.

[24] M. Picher, S. Mazzucco, S. Blankenship, R. Sharma, Vibrational and optical spectroscopies integrated with environmental transmission electron microscopy, Ultramicroscopy. 150 (2015) 10–15, https://doi.org/10.1016/j.ultramic.2014.11.023.

[25] J.C. Idrobo, A.R. Lupini, T. Feng, R.R. Unocic, F.S. Walden, D.S. Gardiner, T. C. Lovejoy, N. Dellby, S.T. Pantelides, O.L. Krivanek, Temperature measurement by a nanoscale electron probe using energy gain and loss spectroscopy, Phys. Rev. Lett. 120 (2018), https://doi.org/10.1103/PhysRevLett.120.095901.

[26] M.J. Lagos, A. Trügler, U. Hohenester, P.E. Batson, Mapping vibrational surface and bulk modes in a single nanocube, Nature 543 (2017) 529–532, https://doi.org/10.1038/nature21699.
[27] T.P. van Swieten, T. van Omme, D.J. van den Heuvel, S.J.W. Vonk, R.G. Spruit, F. Meirer, H.H.P. Garza, B.M. Weckhuysen, A. Meijerink, F.T. Rabouw, R. G. Geitenbeek, Mapping elevated temperatures with a micrometer resolution using the luminescence of chemically stable upconversion nanoparticles, ACS. Appl. Nano Mater. 4 (2021) 4208–4215, https://doi.org/10.1021/acsanm.1c00657.
[28] K.W. Mauser, M. Solà-Garcia, M. Liebtrau, B. Damilano, P.-M. Coulon, S. Vézian, P. A. Shields, S. Meuret, A. Polman, Employing cathodoluminescence for nanothermometry and thermal transport measurements in semiconductor nanowires, ACS. Nano 15 (2021) 11385–11395, https://doi.org/10.1021/acsnano.1c00850.
[29] A. Barker, B. Sapkota, J.P. Oviedo, R. Klie, Automated plasmon peak fitting derived temperature mapping in a scanning transmission electron microscope, AIP. Adv. 11 (2021), https://doi.org/10.1063/5.0039864.
[30] B.C. Regan, W.A. Hubbard, E.R. White, R. Dhall, S.B. Cronin, S. Aloni, M. Mecklenburg, Introduction to plasmon energy expansion thermometry, Microsc. Microanal. 21 (2015) 1907–1908, https://doi.org/10.1017/s1431927615010314.
[31] L. Shen, M. Mecklenburg, R. Dhall, B.C. Regan, S.B. Cronin, Measuring nanoscale thermal gradients in suspended MoS2 with STEM-EELS, Appl. Phys. Lett. 115 (2019), https://doi.org/10.1063/1.5094443.
[32] P. Palanisamy, J.M. Howe, Melting and supercooling studies in submicron Al particles using valence electron energy-loss spectroscopy in a transmission electron microscope, J. Appl. Phys. 110 (2011), https://doi.org/10.1063/1.3609063.
[33] A. Kumar, E. Tiukalova, K. Venkatraman, A. Lupini, J.A. Hachtel, M. Chi, Calibrating cryogenic temperature of TEM specimens using EELS, Ultramicroscopy. 265 (2024), https://doi.org/10.1016/j.ultramic.2024.114008.
[34] W. Hubbard, M. Mecklenburg, B.C. Regan, STEM EBIC thermometry calibration with PEET on al nanoparticles, Microsc. Microanal. (2020), https://doi.org/10.1017/S1431927620023880.
[35] X. Hu, P. Yasaei, J. Jokisaari, S. Öğüt, A. Salehi-Khojin, R.F. Klie, Mapping thermal expansion coefficients in freestanding 2D materials at the nanometer scale, Phys. Rev. Lett. 120 (2018), https://doi.org/10.1103/PhysRevLett.120.055902.
[36] A. Chmielewski, C. Ricolleau, D. Alloyeau, G. Wang, J. Nelayah, Nanoscale temperature measurement during temperature controlled in situ TEM using Al plasmon nanothermometry, Ultramicroscopy. 209 (2020), https://doi.org/10.1016/j.ultramic.2019.112881.
[37] M. Mecklenburg, B. Zutter, B.C. Regan, Thermometry of silicon nanoparticles, Phys. Rev. Appl. 9 (2018), https://doi.org/10.1103/PhysRevApplied.9.014005.
[38] M. Mecklenburg, W.A. Hubbard, E.R. White, R. Dhall, S.B. Cronin, S. Aloni, B.C. Regan, Nanoscale temperature mapping in operating microelectronic devices, 2015. https://www.science.org.
[39] H. Abe, M. Terauchi, M. Tanaka, Temperature dependence of the volume-plasmon energy in silver, 1995.
[40] H. Abe, M. Terauchi, R. Kuzuo, M. Tanaka, Temperature dependence of the volume-plasmon energy in aluminum, 1992.
[41] K. Liao, K. Shibata, T. Mizoguchi, Nanoscale investigation of local thermal expansion at SrTiO3 grain boundaries by electron energy loss spectroscopy, Nano Lett. 21 (2021) 10416–10422, https://doi.org/10.1021/acs.nanolett.1c03735.
[42] C. Kittel, D.F. Holcomb, Introduction to solid state physics, Am. J. Phys. 35 (1967) 547–548, https://doi.org/10.1119/1.1974177.
[43] M.P. Seah, G.C. Smith, Plasmons: quanta for micro-region temperature measurement, 1986.
[44] M. Mitome, Y. Yamazaki, H. Takagi, T. Nakagiri, Size dependence of plasmon energy in Si clusters, J. Appl. Phys. 72 (1992) 812–814, https://doi.org/10.1063/1.351820.
[45] H. Abe, M. Terauchi, R. Kuzuo, M. Tanaka, Temperature dependence of the volume-plasmon energy in aluminum, 1992.
[46] S. Vijayan, J.R. Jinschek, S. Kujawa, J. Greiser, M. Aindow, Focused ion beam preparation of specimens for micro-electro-mechanical system-based transmission electron microscopy heating experiments, Microsc. Microanal. 23 (2017) 708–716, https://doi.org/10.1017/S1431927617000605.
[47] J.J.R. Scott, B. Casals, K.-F. Luo, A. Haq, D. Mariotti, E.K.H. Salje, M. Arredondo, Avalanche criticality in LaAlO$$_3$$ and the effect of aspect ratio, Sci. Rep. 12 (2022) 14818, https://doi.org/10.1038/s41598-022-18390-7.
[48] X. Wang, X. Ma, C. Liao, B. Zhao, High temperature processing of tungsten slag, in: 2020: pp. 289–294. https://doi.org/10.1007/978-3-030-36540-0_26.
[49] J.H. Weaver, C.G. Olson, D.W. Lynch, Optical properties of crystalline tungsten, Phys. Rev. B 12 (1975) 1293–1297, https://doi.org/10.1103/PhysRevB.12.1293.
[50] D.P. Rai, R.K. Thapa, A theoretical study of bulk tungsten (W) based on momentum transfer (q -dependent), Adv. Optics 2014 (2014) 1–9, https://doi.org/10.1155/2014/814909.
[51] R.F. Egerton, Electron energy-loss spectroscopy in the electron microscope, Electron Energy-Loss Spectrosc. Electron Microsc. (2011), https://doi.org/10.1007/978-1-4419-9583-4.
[52] J.T. van Omme, M. Zakhozheva, R.G. Spruit, M. Sholkina, H.H. Pérez Garza, Advanced microheater for in situ transmission electron microscopy; enabling unexplored analytical studies and extreme spatial stability, Ultramicroscopy. 192 (2018) 14–20, https://doi.org/10.1016/j.ultramic.2018.05.005.
[53] T. Malis, S.C. Cheng, R.F. Egerton, EELS log-ratio technique for specimen-thickness measurement in the TEM, J. Electron. Microsc. Tech. 8 (1988) 193–200, https://doi.org/10.1002/jemt.1060080206.
[54] P.C. Martin, Sum rules, Kramers-Kronig relations, and transport coefficients in charged systems, Phys. Rev. 161 (1967) 143–155, https://doi.org/10.1103/PhysRev.161.143.
[55] R.F. Egerton, S.C. Cheng, Measurement of local thickness by electron energy-loss spectroscopy, Ultramicroscopy. 21 (1987) 231–244, https://doi.org/10.1016/0304-3991(87)90148-3.
[56] Digital Micrograph / Gatan Microscopy Suite, Gatan Inc., Pleasanton, CA, USA [Computer software], (n.d.) 3.20.1314.0.
[57] Daen Jannis, joverbee/pyEELSMODEL: v0.1.1 (v0.1.1), Zenodo (2024), https://doi.org/10.5281/zenodo.10992986.
[58] P. Virtanen, R. Gommers, T.E. Oliphant, M. Haberland, T. Reddy, D. Cournapeau, E. Burovski, P. Peterson, W. Weckesser, J. Bright, S.J. van der Walt, M. Brett, J. Wilson, K.J. Millman, N. Mayorov, A.R.J. Nelson, E. Jones, R. Kern, E. Larson, C. J. Carey, İ. Polat, Y. Feng, E.W. Moore, J. VanderPlas, D. Laxalde, J. Perktold, R. Cimrman, I. Henriksen, E.A. Quintero, C.R. Harris, A.M. Archibald, A.H. Ribeiro, F. Pedregosa, P. van Mulbregt, A. Vijaykumar, A. Pietro Bardelli, A. Rothberg, A. Hilboll, A. Kloeckner, A. Scopatz, A. Lee, A. Rokem, C.N. Woods, C. Fulton, C. Masson, C. Häggström, C. Fitzgerald, D.A. Nicholson, D.R. Hagen, D. V. Pasechnik, E. Olivetti, E. Martin, E. Wieser, F. Silva, F. Lenders, F. Wilhelm, G. Young, G.A. Price, G.-L. Ingold, G.E. Allen, G.R. Lee, H. Audren, I. Probst, J. P. Dietrich, J. Silterra, J.T. Webber, J. Slavič, J. Nothman, J. Buchner, J. Kulick, J. L. Schönberger, J.V. de Miranda Cardoso, J. Reimer, J. Harrington, J.L. C. Rodríguez, J. Nunez-Iglesias, J. Kuczynski, K. Tritz, M. Thoma, M. Newville, M. Kümmerer, M. Bolingbroke, M. Tartre, M. Pak, N.J. Smith, N. Nowaczyk, N. Shebanov, O. Pavlyk, P.A. Brodtkorb, P. Lee, R.T. McGibbon, R. Feldbauer, S. Lewis, S. Tygier, S. Sievert, S. Vigna, S. Peterson, S. More, T. Pudlik, T. Oshima, T.J. Pingel, T.P. Robitaille, T. Spura, T.R. Jones, T. Cera, T. Leslie, T. Zito, T. Krauss, U. Upadhyay, Y.O. Halchenko, Y. Vázquez-Baeza, SciPy 1.0: fundamental algorithms for scientific computing in Python, Nat. Methods 17 (2020) 261–272, https://doi.org/10.1038/s41592-019-0686-2.
[59] COMSOL Multiphysics®, COMSOL AB, Stockholm, Sweden, 2018 v. 5.4 www.comsol.com.
[60] S. Bals, W. Tirry, R. Geurts, Z. Yang, D. Schryvers, High-quality sample preparation by Low kV FIB thinning for analytical TEM measurements, Microsc. Microanal. 13 (2007) 80–86, https://doi.org/10.1017/S1431927607070018.
[61] A.P. CONLAN, E. TILLOTSON, A. RAKOWSKI, D. COOPER, S.J. HAIGH, Direct measurement of TEM lamella thickness in FIB-SEM, J. Microsc. 279 (2020) 168–176, https://doi.org/10.1111/jmi.12852.
[62] D.P. Rai, R.K. Thapa, A theoretical study of bulk tungsten (W) based on momentum transfer (q -dependent), Adv. Optics 2014 (2014) 1–9, https://doi.org/10.1155/2014/814909.
[63] J.H. Weaver, C.G. Olson, D.W. Lynch, Optical properties of crystalline tungsten, Phys. Rev. B 12 (1975) 1293–1297, https://doi.org/10.1103/PhysRevB.12.1293.
[64] P.E. Luscher, Energy loss mechanisms in low energy electron scattering from W (100) and their use as a surface sensitive spectroscopy, Surf. Sci. 66 (1977) 167–188, https://doi.org/10.1016/0039-6028(77)90406-X.
[65] Z. Li, J.M. Gong, Y. Harada, B. Da, R.G. Zeng, Z.J. Ding, Determination of the energy loss function of tungsten from reflection electron energy loss spectroscopy spectra, Results. Phys. 56 (2024), https://doi.org/10.1016/j.rinp.2023.107247.
[66] V.Yu. Bodryakov, Correlation of temperature dependences of thermal expansion and heat capacity of refractory metal up to the melting point: tungsten, High Temp. 53 (2015) 643–648, https://doi.org/10.1134/S0018151X15040069.
[67] B.N. Dutta, B. Dayal, Lattice constants and thermal expansion of gold up to 878 °C by X-Ray method, Phys. Status Solidi 3 (1963) 473–477, https://doi.org/10.1002/pssb.19630030312 (b).
[68] G. Botton, Analytical electron microscopy. Science of Microscopy, Springer, New York, New York, NY, 2007, pp. 273–405. doi:10.1007/978-0-387-49762-4_4.
[69] J. Palisaitis, C.-L. Hsiao, M. Junaid, J. Birch, L. Hultman, P.O.Å. Persson, Effect of strain on low-loss electron energy loss spectra of group-III nitrides, Phys. Rev. B 84 (2011) 245301, https://doi.org/10.1103/PhysRevB.84.245301.
[70] A.I. Oliva, J.M. Lugo, R.A. Gurubel-Gonzalez, R.J. Centeno, J.E. Corona, F. Avilés, Temperature coefficient of resistance and thermal expansion coefficient of 10-nm thick gold films, Thin. Solid. Films. 623 (2017) 84–89, https://doi.org/10.1016/j.tsf.2016.12.028.
[71] A.I. Oliva, L. Ruiz-Tabasco, J. Ojeda-García, J.E. Corona, V. Sosa, F. Avilés, Effects of temperature and tensile strain on the electrical resistance of nanometric gold films, Mater. Res. Express. 6 (2019) 066407, https://doi.org/10.1088/2053-1591/ab0c43.
[72] S. Pathak, V.B. Shenoy, Size dependence of thermal expansion of nanostructures, Phys. Rev. B 72 (2005) 113404, https://doi.org/10.1103/PhysRevB.72.113404.
[73] S.J. Pennycook, Imaging in the STEM. Transmission Electron Microscopy, Springer International Publishing, Cham, 2016, pp. 283–342, https://doi.org/10.1007/978-3-319-26651-0_11.